

Orbital- and spin-driven lattice instabilities in quasi-one-dimensional CaV_2O_4

T. Watanabe^{1,*}, S. Kobayashi¹, Y. Hara², J. Xu³, B. Lake³, J.-Q. Yan^{4,†}, A. Niazi^{4,‡} and D. C. Johnston^{4,5}

¹*Department of Physics, College of Science and Technology (CST),
Nihon University, Chiyoda, Tokyo 101-8308, Japan*

²*National Institute of Technology, Ibaraki College, Hitachinaka 312-8508, Japan*

³*Helmholtz-Zentrum Berlin für Materialien und Energie,
Hahn-Meitner-Platz 1, D-14109 Berlin, Germany*

⁴*Ames Laboratory, Iowa State University, Ames, Iowa 50011, USA and*

⁵*Department of Physics and Astronomy, Iowa State University, Ames, Iowa 50011, USA*

(Dated: February 12, 2022)

Calcium vanadate CaV_2O_4 has a crystal structure of quasi-one-dimensional zigzag chains composed of orbital-active V^{3+} ions and undergoes successive structural and antiferromagnetic phase transitions at $T_s \sim 140$ K and $T_N \sim 70$ K, respectively. We perform ultrasound velocity measurements on a single crystal of CaV_2O_4 . The temperature dependence of its shear elastic moduli exhibits huge Curie-type softening upon cooling that emerges above and below T_s depending on the elastic mode. The softening above T_s suggests the presence of either onsite Jahn-Teller-type or intersite ferro-type orbital fluctuations in the two inequivalent V^{3+} zigzag chains. The softening below T_s suggests the occurrence of a dimensional spin-state crossover, from quasi-one to three, that is driven by the spin-lattice coupling along the inter-zigzag-chain orthogonal direction. The successive emergence of the orbital- and spin-driven lattice instabilities above and below T_s , respectively, is unique to the orbital-spin zigzag chain system of CaV_2O_4 .

PACS numbers: 62.20.de, 75.25.Dk, 75.47.Lx, 75.70.Tj

I. INTRODUCTION

Orbitally degenerate frustrated magnets have attracted considerable interest because they display a variety of complex ground states with unusual magnetic and orbital orders [1]. The prototypical examples are vanadate spinels AV_2O_4 with divalent A^{2+} ions such as Zn^{2+} , Mg^{2+} , and Cd^{2+} , where the trivalent magnetic V^{3+} ions are characterized by double occupancy of the triply degenerate t_{2g} orbitals, and form a pyrochlore lattice. With cooling, the vanadate spinels undergo successive structural and antiferromagnetic (AF) phase transitions at a temperature T_s and a lower temperature $T_N < T_s$ [2–4]. For AV_2O_4 , the structural phase transition is understood to arise from a long-range ordering of the V t_{2g} orbitals in which the lowering of the lattice symmetry results in the release of frustration (magnetic ordering).

Unlike the vanadate spinels AV_2O_4 , calcium vanadate CaV_2O_4 crystallizes in the orthorhombic CaFe_2O_4 -type structure (space group $Pnam$) at room temperature, which consists of the two inequivalent V^{3+} zigzag chains running along the crystal c axis [Fig. 1(a)]. Let V1 and V2 denote the inequivalent V sites. The magnetic V^{3+} ions on the V1 and V2 sites possess spin $S = 1$ because of two unpaired $3d$ electrons, where magnetism is dominated by AF interactions [5–7]. With the V1 and V2 zigzag chains consisting of V^{3+} triangular loops, CaV_2O_4 is expected to be a quasi-one-dimensional frustrated magnet.

In CaV_2O_4 , the V^{3+} ions are surrounded by slightly distorted O octahedra, which share edges within the V1 and V2 zigzag chains but share corners between the V1 and V2 zigzag chains [Fig. 1(b)]. The trivalent magnetic V^{3+} ion in the octahedral O environment is char-

acterized by double occupancy of the triply-degenerate t_{2g} orbitals. In CaV_2O_4 with the high-temperature orthorhombic crystal structure, the octahedral O environment is tetragonally compressed, and the t_{2g} orbitals are split into a lower nondegenerate d_{xy} orbital and higher doubly-degenerate d_{yz} and d_{zx} orbitals [Fig. 2(a)] [7,8]. Therefore, although the O octahedra in the orthorhombic CaV_2O_4 is slightly distorted, the V^{3+} ions should have an orbital degree of freedom [Fig. 2(a)]; the lower d_{xy} orbital is occupied by one of the two electrons, and the higher doubly-degenerate d_{yz} and d_{zx} orbitals are partially occupied by the remaining one electron. Fig.

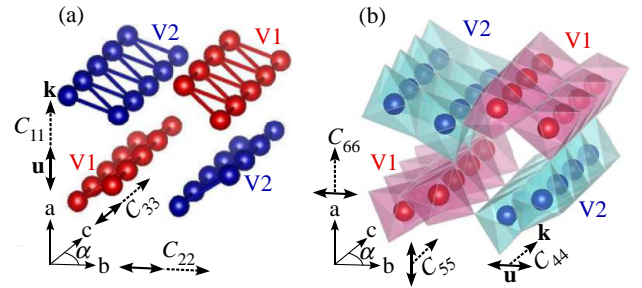


FIG. 1: (Color online) Bonding network in the crystal structure of CaV_2O_4 : (a) V atoms and (b) VO_6 octahedra. In (a) and (b), V1 and V2 denote the inequivalent V sites. The angle α displayed in the crystal axes corresponds to the monoclinic angle in the monoclinic crystal phase below T_s [6]. In (a), the propagation vector \mathbf{k} and polarization vector \mathbf{u} of the longitudinal sound waves for C_{11} , C_{22} , and C_{33} are indicated. In (b), the propagation vector \mathbf{k} and polarization vector \mathbf{u} of the transverse sound waves for C_{44} , C_{55} , and C_{66} are indicated.

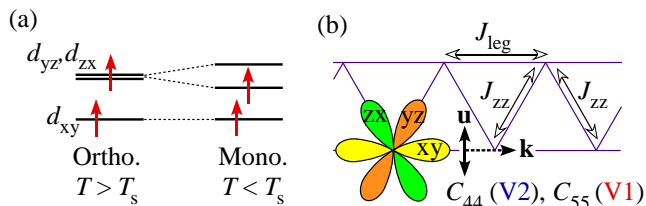


FIG. 2: (Color online) (a) Schematic t_{2g} energy levels of V^{3+} $3d^2$ electrons in the orthorhombic (left) and monoclinic (right) crystal phases of CaV_2O_4 . (b) Schematic of the V t_{2g} orbitals in the zigzag chain of CaV_2O_4 . In (b), two competing AF interactions of the nearest-neighbor J_{zz} along the zigzags and the next-nearest-neighbor J_{leg} along the leg are indicated. Additionally, the propagation vector \mathbf{k} and polarization vector \mathbf{u} of the transverse sound wave corresponding to the $\epsilon_{xx} - \epsilon_{yy}$ elastic mode (d_{yz}/d_{zx} -active mode) for the t_{2g} orbitals are indicated. For the V1 and V2 zigzag chains of CaV_2O_4 , C_{55} and C_{44} , respectively, correspond to this elastic mode.

2(b) depicts a schematic of the V t_{2g} orbitals in the zigzag chain of CaV_2O_4 . The nondegenerate d_{xy} orbital aligns with the leg direction of the zigzag chain, but the doubly-degenerate d_{yz} and d_{zx} orbitals align to the zigzag directions. In CaV_2O_4 , its magnetism is understood to be dominated by two competing AF interactions of the nearest-neighbor J_{zz} along the zigzags and the next-nearest-neighbor J_{leg} along the leg [Fig. 2(b)]. Hence, the ground state of CaV_2O_4 has attracted interest as a quasi-one-dimensional orbitally degenerate frustrated magnet [5–7,9–14].

CaV_2O_4 undergoes successive structural and magnetic phase transitions; a weak orthorhombic-to-monoclinic lattice distortion at a temperature $T_s \sim 140$ K, and an AF ordering at a lower temperature $T_N \sim 70$ K, $T_s > T_N$ [5–7]. In the monoclinic crystal structure below T_s , the monoclinic angle is between the b and c axes (α) of the orthorhombic crystal structure above T_s [Figs. 1(a) and 1(b)], which evolves continuously below T_s and saturates at $\alpha \simeq 89.2^\circ$ at low temperatures [6,7,15]. Moreover, the structural distortion below T_s lifts the orbital degeneracy [Fig. 2(a)]. From the magnetic susceptibility and the neutron scattering measurements in the single crystal of CaV_2O_4 , each zigzag spin chain of this compound [Fig. 2(b)] evidently changes state at T_s from the J_{leg} -dominant Haldane-chain state above T_s to the J_{leg}/J_{zz} -competing spin-ladder state below T_s , which results from the J_{zz} enhancement driven by a ferro-type ordering of the d_{yz}/d_{zx} orbitals below T_s [7].

Below T_N , CaV_2O_4 exhibits a three-dimensional AF order with a propagation vector $\mathbf{Q} = (0, \frac{1}{2}, \frac{1}{2})$ despite the quasi-one-dimensional character of the crystal structure [5–7,16–18]. Here, the AF structure consists of collinear V1/V2 zigzag chains that are canted with respect to each other [5,7], where the ordered magnetic moment of $1.0\mu_B \leq \mu \leq 1.59\mu_B$ reduced from $2\mu_B$ for $S = 1$ is considered to arise from the low-dimensional and/or frustrated magnetic character [5–7,16–18]. For CaV_2O_4 , the

orbital ordering at T_s in the V^{3+} zigzag chains is believed to lead to the three-dimensional AF ordering (due to the release of frustration) at the lower T_N .

In this paper, we present ultrasound velocity measurements of the quasi-one-dimensional orbital degenerate CaV_2O_4 , from which we determine the elastic moduli of this compound. The elastic modulus of a crystal is a thermodynamic tensor quantity, and therefore the ultrasound velocity measurements of the symmetrically independent elastic moduli in a crystal can provide symmetry-resolved thermodynamic information. In magnets, the modified sound dispersions caused by magnetoelastic coupling allow one to extract detailed information about the interplay of the lattice, spin, and orbital degrees of freedom [19–29]. For CaV_2O_4 , we find two different types of orbital-driven elastic anomalies in the orthorhombic paramagnetic (PM) phase above T_s , and a spin-driven elastic anomaly in the lower-temperature monoclinic PM phase below T_s that are observed in the symmetrically different elastic modes. These elastic anomalies should be precursors to successive occurrences of the orbital order at T_s and the spin order at the lower T_N , a feature which is unique to the orbital-spin zigzag chain system of CaV_2O_4 .

II. EXPERIMENTAL

Single crystals of CaV_2O_4 with $T_s \sim 140$ K and $T_N \sim 70$ K were grown by the floating-zone method [6]. The ultrasound velocity measurements were performed using the phase-comparison technique with longitudinal and transverse sound waves at a frequency of 30 MHz. The ultrasound waves were generated and detected by LiNbO_3 transducers glued on the parallel mirror surfaces of the crystal which are respectively perpendicular to the a , b , and c orthorhombic axes. Measurements were taken to determine the symmetrically independent elastic moduli in the orthorhombic crystal, specifically, C_{11} , C_{22} , C_{33} , C_{44} , C_{55} , and C_{66} (see Table I). In Figs. 1(a) and 1(b), the propagation vector \mathbf{k} and polarization vector \mathbf{u} of the sound waves for the respective elastic moduli are indicated along with the bonding network of CaV_2O_4 crystal. As indicated in Fig. 1(a), the longitudinal sound wave corresponding to the compressive elastic modulus C_{33}

TABLE I: Elastic moduli for CaV_2O_4 with the orthorhombic crystal structure, and the corresponding sound mode (propagation vector \mathbf{k} and polarization vector \mathbf{u}) and symmetry.

Elastic modulus	Sound mode (\mathbf{k} and \mathbf{u})	Symmetry
C_{11}	Longitudinal wave ($\mathbf{k} \parallel \mathbf{u} \parallel \mathbf{a}$)	A_g
C_{22}	Longitudinal wave ($\mathbf{k} \parallel \mathbf{u} \parallel \mathbf{b}$)	A_g
C_{33}	Longitudinal wave ($\mathbf{k} \parallel \mathbf{u} \parallel \mathbf{c}$)	A_g
C_{44}	Transverse wave ($\mathbf{k} \parallel \mathbf{c}, \mathbf{u} \parallel \mathbf{b}$)	B_{3g}
C_{55}	Transverse wave ($\mathbf{k} \parallel \mathbf{c}, \mathbf{u} \parallel \mathbf{a}$)	B_{2g}
C_{66}	Transverse wave ($\mathbf{k} \parallel \mathbf{a}, \mathbf{u} \parallel \mathbf{b}$)	B_{1g}

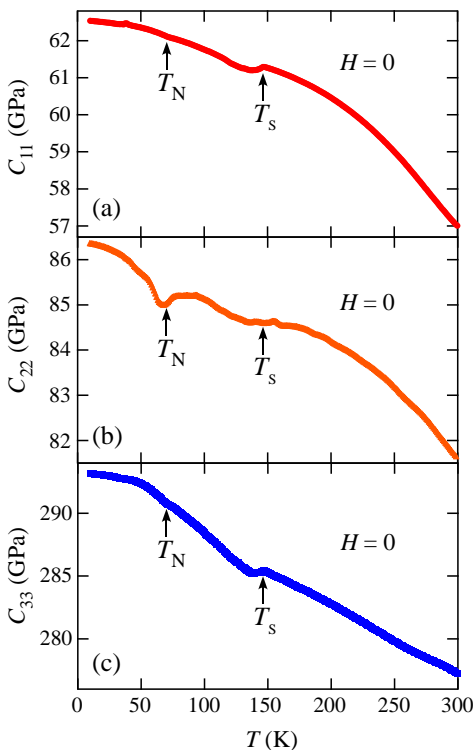


FIG. 3: (Color online) Compressive elastic moduli of CaV_2O_4 as functions of temperature. (a) $C_{11}(T)$, (b) $C_{22}(T)$, and (c) $C_{33}(T)$. The labelled arrows indicate T_s and T_N .

propagates along the V1 and V2 chains ($\mathbf{k} \parallel \mathbf{c}$), whereas the longitudinal waves corresponding to the compressive C_{11} and C_{22} propagate orthogonal to the V1 and V2 chains ($\mathbf{k} \perp \mathbf{c}$). Likewise, in Fig. 1(b), the transverse sound waves corresponding to the shear elastic moduli C_{44} and C_{55} propagate along the V1 and V2 chains ($\mathbf{k} \parallel \mathbf{c}$), whereas the transverse wave corresponding to the shear C_{66} propagates orthogonal to the V1 and V2 chains ($\mathbf{k} \perp \mathbf{c}$). The sound velocities of CaV_2O_4 measured at room temperature (300 K) are 3510 m/s for C_{11} , 4200 m/s for C_{22} , 7740 m/s for C_{33} , 2970 m/s for C_{44} , 3620 m/s for C_{55} , and 4380 m/s for C_{66} .

III. RESULTS

The temperature (T) dependence of the compressive elastic moduli $C_{11}(T)$, $C_{22}(T)$, and $C_{33}(T)$, respectively, in CaV_2O_4 all exhibit small discontinuous changes at T_s and T_N [marked by arrows in Figs. 3(a)-3(c)]. In regard to the magnetostructural phases of CaV_2O_4 , specifically, the orthorhombic PM phase ($T > T_s$), monoclinic PM phase ($T_N < T < T_s$), and monoclinic AF phase ($T < T_N$), all three compressive elastic moduli exhibit monotonic hardening upon cooling, as is usually observed in solids [30].

In contrast to the compressive elastic moduli (Fig.

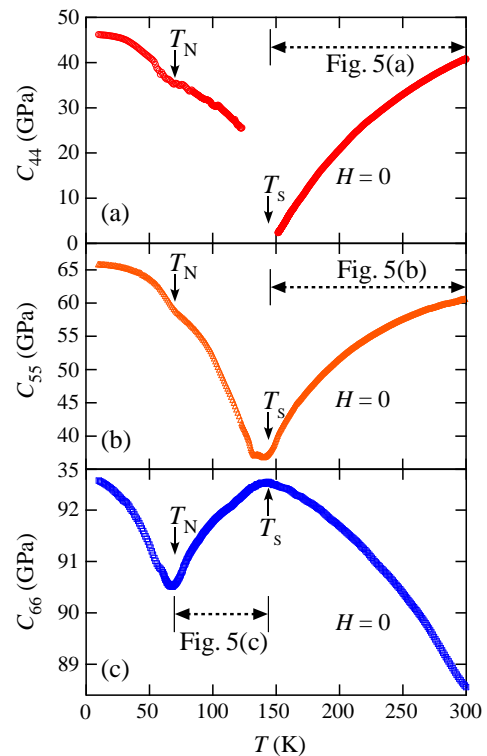


FIG. 4: (Color online) Shear elastic moduli of CaV_2O_4 as functions of temperature. (a) $C_{44}(T)$, (b) $C_{55}(T)$, and (c) $C_{66}(T)$. The labelled arrows indicate T_s and T_N . The experimental data in the temperature ranges indicated by double-headed arrows are displayed rescaled in Fig. 5.

3), the shear elastic moduli of CaV_2O_4 are found to exhibit unusual temperature variations that depend on the elastic mode. Figure 4 gives the temperature dependence of the shear elastic moduli $C_{44}(T)$, $C_{55}(T)$, and $C_{66}(T)$ in CaV_2O_4 . In the orthorhombic PM phase ($T > T_s$), $C_{44}(T)$ [Fig. 4(a)] and $C_{55}(T)$ [Fig. 4(b)] exhibit huge Curie-type ($\sim -1/T$ -type) softening upon cooling, whereas $C_{66}(T)$ [Fig. 4(c)] exhibits ordinary hardening. Conversely, in the monoclinic PM phase ($T_N < T < T_s$), $C_{66}(T)$ [Fig. 4(c)] exhibits Curie-type softening upon cooling, whereas $C_{44}(T)$ [Fig. 4(a)] and $C_{55}(T)$ [Fig. 4(b)] exhibit hardening upon cooling. Here, it is impossible to measure $C_{44}(T)$ below T_s down to ~ 125 K [Fig. 4(a)] because the ultrasound signal damped strongly. In the monoclinic AF phase ($T < T_N$), $C_{44}(T)$, $C_{55}(T)$, and $C_{66}(T)$ all exhibit hardening upon cooling (Fig. 4). For the shear elastic moduli of CaV_2O_4 , T_s and T_N intriguingly correspond to the elastic-mode-dependent softening-hardening turning points (Fig. 4). In the next section, we shall discuss the origin of the elastic-mode-dependent unusual temperature variations of the shear elastic moduli.

In the present study, we measured $C_{11}(T) \sim C_{66}(T)$ not only in the absence of a magnetic field [Figs. 3 and 4], but also with magnetic fields up to 7 T. We find an

absence of a magnetic field effect on any of the elastic properties.

IV. DISCUSSION

The present experimental results reveal that, in CaV_2O_4 , while symmetry-conserving isotropic elastic modes of the compressive moduli $C_{11}(T)$, $C_{22}(T)$, and $C_{33}(T)$ exhibit ordinal hardening upon cooling (Fig. 3), symmetry-lowering anisotropic elastic modes of the shear moduli $C_{44}(T)$, $C_{55}(T)$, and $C_{66}(T)$ exhibit unusual elastic-mode-dependent temperature variations (Fig. 4). These elastic properties should reflect the low-dimensional orbital and spin characters of this compound, which strongly couple to the lattice. From here on, we shall discuss the origin of these unusual temperature variations in $C_{44}(T)$, $C_{55}(T)$, and $C_{66}(T)$.

First we address the origin of Curie-type softening in $C_{44}(T)$ and $C_{55}(T)$ in the orthorhombic PM phase ($T > T_s$) [Figs. 4(a) and 4(b)]. This elastic instability is quenched below T_s , and therefore should be a precursor to the structural transition at T_s lifting the orbital degeneracy of V^{3+} ions [Fig. 2(a)].

In an orbital-degenerate system, the temperature dependence of the elastic modulus $C_\Gamma(T)$ above the structural transition temperature is explained by assuming the coupling of the ultrasound to the orbital-degenerate ions through the onsite orbital-strain (quadrupole-strain) interaction, and the presence of the intersite orbital-orbital (quadrupole-quadrupole) interaction. [19–22]. A mean-field expression of $C_\Gamma(T)$ for the orbital-degenerate system is given as

$$C_\Gamma(T) = C_\Gamma^0 \frac{T - T_c}{T - \theta}, \quad (1)$$

with C_Γ^0 the background elastic constant, T_c the second-order critical temperature for elastic softening $C_\Gamma \rightarrow 0$, and θ the intersite orbital-orbital interaction. The difference of the two characteristic temperatures $T_c - \theta$ is the energy gain from the onsite orbital-strain interaction, which corresponds to the onsite Jahn-Teller coupling energy E_{JT} with $T_c - \theta = E_{JT}$. θ is positive (negative) when the interaction is ferro-distortive (antiferro-distortive). The ferro-distortive (antiferro-distortive) interaction is expected to lead to a ferro-orbital order (antiferro-orbital order) with (without) a macroscopic lattice distortion.

Fits of the experimental $C_{44}(T)$ and $C_{55}(T)$ to Eq. (1) for $T > T_s$ [Figs. 5(a) and 5(b); solid black curves] reproduce very well the experimental data. Values for the fitting parameters are also presented. The larger E_{JT} in $C_{44}(T)$ than in $C_{55}(T)$ indicates that the strain for C_{44} generates a stronger onsite orbital-strain interaction than the strain for C_{55} . The change in sign of θ between $C_{44}(T)$ and $C_{55}(T)$ indicates the coexistence of different types of intersite orbital-orbital interactions. Moreover,

the larger magnitude of θ in $C_{55}(T)$ than in $C_{44}(T)$ indicates that the intersite orbital-orbital interaction affecting $C_{55}(T)$ is stronger than that affecting $C_{44}(T)$.

For CaV_2O_4 , the monoclinic angle in the low-temperature monoclinic crystal structure is between the b and c axes (α) of the high-temperature orthorhombic crystal structure [6]; see Fig. 5(a). Hence, with C_{44} corresponding to the α tilt mode ($\mathbf{k} \parallel \mathbf{c}$ and $\mathbf{u} \parallel \mathbf{b}$), Curie-type softening in $C_{44}(T)$ above T_s should be a precursor to the orthorhombic-to-monoclinic lattice distortion at T_s . If E_{JT} is much stronger than θ in $C_{44}(T)$ [Fig. 5(a)], the orthorhombic-to-monoclinic lattice distortion at T_s

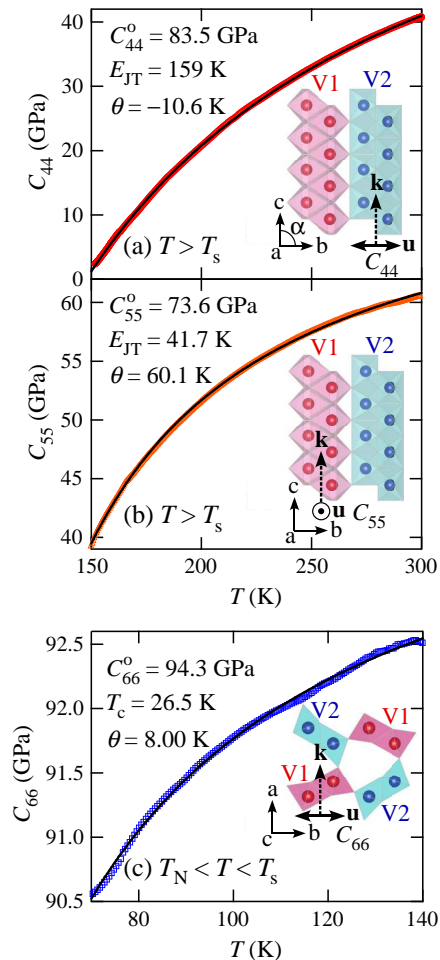


FIG. 5: (Color online) Expanded view of the shear elastic moduli for CaV_2O_4 given in from Fig. 4: (a) $C_{44}(T)$ in the orthorhombic PM phase ($T > T_s$), (b) $C_{55}(T)$ in the orthorhombic PM phase ($T > T_s$), and (c) $C_{66}(T)$ in the monoclinic PM phase ($T_N < T < T_s$). The solid black curves in all three plots are fits using Eq. (1) of the experimental data; values for the fitting parameters are also listed. The VO_6 octahedra of the V1 and V2 zigzag chains are illustrated along with the sound propagation vector \mathbf{k} and polarization vector \mathbf{u} . In (a), the angle α displayed in the crystal axes corresponds to the monoclinic angle in the monoclinic crystal phase ($T < T_s$) [6].

in CaV_2O_4 should be a Jahn-Teller-type lattice distortion, where the onsite orbital-strain interaction lifts the orbital degeneracy.

Distinct from C_{44} , the strain generated by ultrasound in C_{55} ($\mathbf{k} \parallel \mathbf{c}$ and $\mathbf{u} \parallel \mathbf{a}$) tilts the angle between the c and a axes of the orthorhombic crystal structure [Fig. 5(b)]. Therefore, Curie-type softening in $C_{55}(T)$ above T_s should be an elastic instability rather than the precursor to the bc -plane monoclinic lattice distortion at T_s . With the strong positive θ in $C_{55}(T)$ [Fig. 5(b)], Curie-type softening in $C_{55}(T)$ should be a precursor to an orbital ordering, where the intersite ferro-orbital interactions play an important role. At T_s , a small monoclinic lattice distortion within the ac -plane might coincide with a larger distortion within the bc -plane, which has not been experimentally identified so far.

We here note that, in CaV_2O_4 , the inequivalent V1 and V2 sites each have different crystal-field z directions of the $3d$ orbitals, specifically, close to the crystal b axis (a axis) in the V1 (V2) sites [7,14]. For the t_{2g} orbitals of the d electrons, the strain $\epsilon_{xx} - \epsilon_{yy}$ generated by transverse sound waves does not change the energy level of d_{xy} orbital, but lowers/raises the energy levels of d_{yz} and d_{zx} orbitals, respectively. In CaV_2O_4 , C_{44} corresponds to such a d_{yz}/d_{zx} -active elastic mode for the V2 sites [Figs. 2(b) and 5(a)], and C_{55} for the V1 sites [Figs. 2(b) and 5(b)]. Therefore, in CaV_2O_4 , the strain generated by ultrasound should couple to the d_{yz} and d_{zx} orbitals of the V2 sites in regard to C_{44} and the V1 sites in regard to C_{55} . Given the fitted parameter values of E_{JT} and θ [Figs. 5(a) and 5(b)], Curie-type softening in $C_{44}(T)$ and $C_{55}(T)$ should be driven by two different types of orbital fluctuations: respectively, onsite Jahn-Teller-type orbital fluctuations in the V2 sites affecting $C_{44}(T)$ and intersite ferro-orbital fluctuations in the V1 sites affecting $C_{55}(T)$. Consequently, the observation of Curie-type softening in $C_{44}(T)$ and $C_{55}(T)$ above T_s suggests that, at T_s , the Jahn-Teller-type orbital ordering occurs in the V2 sites, but another type of orbital ordering driven by the intersite ferro-orbital interactions occurs in the V1 sites. Here, the coincidental occurrence at T_s of the two different types of orbital ordering at the respective V1 and V2 sites indicates that these orbital orderings are a cooperative phenomenon arising from the weak coupling of the two inequivalent V1 and V2 zigzag chains. Below T_s , the ferro-type orbital configurations should form in the inequivalent V1 and V2 zigzag chains [Fig. 6(a)]. These orbital configurations are compatible with the emergence of the spin-ladder state below T_s in each zigzag spin chain, as indicated from the magnetic susceptibility and neutron scattering measurements [7].

Next we discuss the origin of Curie-type softening in $C_{66}(T)$ in the monoclinic PM phase ($T_N < T < T_s$) [Fig. 4(c)]. Note that, in the monoclinic PM phase ($T_N < T < T_s$), $C_{44}(T)$ and $C_{55}(T)$ exhibit ordinal hardening upon cooling [Figs. 4(a) and 4(b)], which indicates that the orbital degeneracies of the V1 and V2 sites are both lifted below T_s . Thus, taking into account that $C_{66}(T)$ exhibits

ordinal hardening upon cooling in the orthorhombic PM phase ($T > T_s$) [Fig. 4(c)], the emergence of Curie-type softening in $C_{66}(T)$ in the monoclinic PM phase ($T_N < T < T_s$) should be the result of the generation of a new spin-lattice coupling in this phase, which is driven by the orbital ordering at T_s . Additionally, note that Curie-type softening in $C_{66}(T)$ is quenched below T_N [Fig. 4(c)]. This indicates that the elastic instability of C_{66} in the monoclinic PM phase ($T_N < T < T_s$) is a precursor to the AF transition at T_N .

In a spin-lattice coupled system, the temperature dependence of the elastic modulus $C_\Gamma(T)$ is explained by assuming a coupling of ultrasound with the magnetic ions through the magnetoelastic coupling acting on the exchange interactions, where the exchange striction arises from an ultrasound modulation of the exchange interactions [19,28,29]. In analogy to the orbital-degenerate system, Curie-type softening in $C_\Gamma(T)$ in the spin-lattice coupled system is explained by assuming the coupling of ultrasound to the magnetic ions via the exchange striction mechanism, and the presence of exchange-striction-sensitive intersite spin-spin interactions. The mean-field expression of the soft mode $C_\Gamma(T)$ for the spin-lattice coupled system should have the same form as in Eq. (1) with C_Γ^0 the background elastic constant, T_c the second-order critical temperature for elastic softening $C_\Gamma \rightarrow 0$, and θ the exchange-striction-sensitive intersite spin-spin interaction [19,28,29].

In Fig. 5(c), a fit of the experimental $C_{66}(T)$ to Eq. (1) in $T_N < T < T_s$ is drawn as a solid black curve, which reproduces very well the experimental data. Values for the fit parameters are also presented. The fitted parameter value of T_c is lower than the experimentally observed Néel temperature T_N , $T_c < T_N$, indicating that the phase transition at T_N is of first order. Taking into

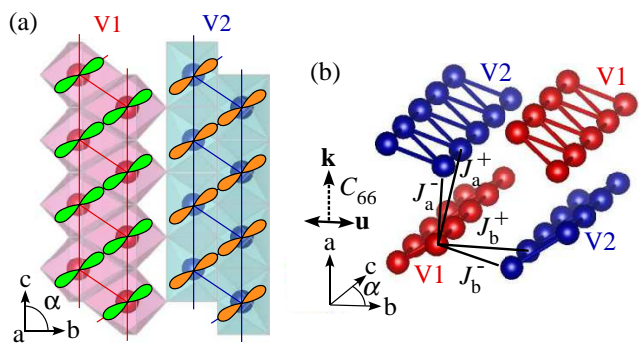


FIG. 6: (Color online) (a) Ferro-type orbital configuration of CaV_2O_4 projected onto the bc plane, which displays VO_6 octahedra of the V1 and V2 zigzag chains. (b) V1 and V2 bonding networks indicating the inter-zigzag-chain neighboring exchange interactions J_a^\pm and J_b^\pm . In (a) and (b), angle α shown with the crystal axes corresponds to that in the monoclinic crystal phase ($T < T_s$) [6]. In (b), the sound propagation vector \mathbf{k} and polarization vector \mathbf{u} for C_{66} tilts the angle between the a and b axes.

account that the second-order transition at T_N was suggested from the thermal expansion measurements [6], the transition at T_N might be of weak first order. The positive fitted value of θ indicates the dominance of ferro-distortive intersite spin-spin interactions.

In CaV_2O_4 , the ultrasound for C_{66} generates the strain within the ab plane, which is orthogonal to both the V1 and V2 zigzag chains [Fig. 5(c)]. Therefore the emergence of the precursor softening to the AF transition in $C_{66}(T)$ indicates that the three-dimensional AF ordering is driven in the quasi-one-dimensional spin system via the spin-lattice coupling along the inter-zigzag-chain orthogonal direction. That is, the generation of this "orthogonal-type" spin-lattice coupling in the monoclinic PM phase ($T_N < T < T_s$) should give rise to a spin-state crossover from quasi-one-dimension to three-dimensions, a feature which is unique to the orbital-spin zigzag chain system of CaV_2O_4 .

For the three-dimensional AF ordering in CaV_2O_4 , the inter-zigzag-chain exchange interactions should play a crucial role via the "orthogonal-type" spin-lattice coupling. As evident in Fig. 6(b), there are two types of inter-zigzag-chain neighboring exchange interactions in CaV_2O_4 : a -axis stacking J_a^\pm and b -axis stacking J_b^\pm . Curie-type softening in $C_{66}(T)$ indicates that J_a^\pm and J_b^\pm in the monoclinic PM phase ($T_N < T < T_s$) are sensitive to the monoclinic lattice deformation within the ab plane [Fig. 6(b)]. Note here that the tilting of the monoclinic angle α below T_s makes the b -axis stacking J_b^+ and J_b^- become inequivalent, although the magnitude of the α tilting is very small [6]. Thus, strictly speaking, Curie-type softening in $C_{66}(T)$ should be driven by J_a^\pm and the slightly inequivalent J_b^+ and J_b^- . For CaV_2O_4 , it is expected that a small monoclinic lattice distortion within the ab plane coincides with AF ordering, although the additional lattice distortion below T_N has not been experimentally observed so far.

V. SUMMARY

Ultrasound velocity measurements of CaV_2O_4 have revealed the elastic-mode-dependent emergence of Curie-type softening above and below T_s in the temperature dependence of the shear elastic moduli $C_{44}(T)$ and $C_{55}(T)$ in the orthorhombic PM phase ($T > T_s$), and $C_{66}(T)$ in the monoclinic PM phase ($T_N < T < T_s$). Softening in $C_{44}(T)$ and $C_{55}(T)$ above T_s can be attributed to the presence of onsite Jahn-Teller-type and intersite ferro-type orbital fluctuations, which arise respectively in the inequivalent V2 and V1 sites. Softening in $C_{66}(T)$ below T_s can be attributed to a dimensional spin-state crossover, from quasi-one-dimension to three-dimensions, driven by the spin-lattice coupling along the inter-zigzag-chain orthogonal direction. Further experimental and theoretical studies are indispensable if the orbital-lattice order below T_s and the spin-lattice order below T_N in the unique orbital-spin zigzag chain system of CaV_2O_4 are to be revealed.

VI. ACKNOWLEDGMENTS

This work was partly supported by Grant-in-Aid for Scientific Research (C) (Grant No. 17K05520) from MEXT of Japan, and by Nihon University College of Science and Technology Grant-in-Aid for Research. The research at Ames Laboratory was supported by the U.S. Department of Energy, Office of Basic Energy Sciences, Division of Materials Sciences and Engineering. Ames Laboratory is operated for the U.S. Department of Energy by Iowa State University under Contract No. DE-AC02-07CH11358.

* Electronic address: tadataka@phys.cst.nihon-u.ac.jp

† Present address: Materials Science and Technology Division, Oak Ridge National Laboratory, Oak Ridge, Tennessee 37831, USA

‡ Present address: Department of Physics, Jamia Millia Islamia, New Delhi 110025, India

¹ P. G. Radaelli, *New J. Phys.* **7**, 53 (2005).

² S.-H. Lee, D. Louca, H. Ueda, S. Park, T. J. Sato, M. Isobe, Y. Ueda, S. Rosenkranz, P. Zschack, J. Íñiguez, Y. Qiu, and R. Osborn, *Phys. Rev. Lett.* **93**, 156407 (2004).

³ H. Mamiya, M. Onoda, T. Furubayashi, J. Tang, and I. Nakatani, *J. Appl. Phys.* **81**, 5289 (1997).

⁴ G. Giovannetti, A. Stroppa, S. Picozzi, D. Baldomir, V. Pardo, S. Blanco-Canosa, F. Rivadulla, S. Jodlauk, D. Niermann, J. Rohrkamp, T. Lorenz, S. Streltsov, D. I. Khomskii, and J. Hemberger, *Phys. Rev. B* **83**, 060402(R) (2011).

⁵ X. Zong, B. J. Suh, A. Niazi, J. Q. Yan, D. L. Schlagel, T. A. Lograsso, and D. C. Johnston, *Phys. Rev. B* **77**, 014412

(2008).

⁶ A. Niazi, S. L. Bud'ko, D. L. Schlagel, J. Q. Yan, T. A. Lograsso, A. Kreyssig, S. Das, S. Nandi, A. I. Goldman, A. Honecker, R. W. McCallum, M. Reehuis, O. Pieper, B. Lake, and D. C. Johnston, *Phys. Rev. B* **79**, 104432 (2009).

⁷ O. Pieper, B. Lake, A. Daoud-Aladine, M. Reehuis, K. Prokeš, B. Klemke, K. Kiefer, J. Q. Yan, A. Niazi, D. C. Johnston, and A. Honecker, *Phys. Rev. B* **79**, 180409(R) (2009).

⁸ See EPAPS Document No. E-PRBMDO-79-R17918 for supplementary information. For more information on EPAPS, see <http://www.aip.org/pubservs/epaps.html>

⁹ H. Kikuchi, M. Chiba, and T. Kubo, *Can. J. Phys.* **79**, 1551 (2001).

¹⁰ G. W. Chern and N. Perkins, *Phys. Rev. B* **80**, 220405(R) (2009).

¹¹ G. W. Chern, N. Perkins, and G. I. Japaridze, *Phys. Rev. B* **82**, 172408 (2010).

¹² A. Nersisyan, G. W. Chern, and N. B. Perkins, *Phys. Rev.*

- B **83**, 205132 (2011).
- ¹³ E. Sela and R. G. Pereira, Phys. Rev. B **84**, 014407 (2011).
- ¹⁴ Z. V. Pchelkina and I. V. Solovyev, J. Phys.: Condens. Matter **27**, 026001 (2015).
- ¹⁵ According to Ref. [⁶], the relative changes of the orthorhombic axis lengths in the monoclinic crystal phase are at most on the order of $\sim 10^{-5}$ for $\Delta a/a$ and $\Delta b/b$, and $\sim 10^{-4}$ for $\Delta c/c$.
- ¹⁶ J. M. Hastings, L. M. Corliss, W. Kunmann, and S. La Placa, J. Phys. Chem. Solids **28**, 1089 (1967).
- ¹⁷ E. F. Bertaut and N. van Nhung, C. R. Seances Acad. Sci., Ser. B **264**, 1416 (1967).
- ¹⁸ J. Sugiyama, Y. Ikedo, T. Goko, E. J. Ansaldo, J. H. Brewer, P. L. Russo, K. H. Chow, and H. Sakurai, Phys. Rev. B **78**, 224406 (2008).
- ¹⁹ B. Lüthi, *Physical Acoustics in the Solid State* (Springer, 2005).
- ²⁰ Y. Kino, Lüthi, and M. E. Mullen, J. Phys. Soc. Jpn. **33**, 687 (1972); Solid State Commun. **12**, 275 (1973).
- ²¹ M. Kataoka and J. Kanamori, J. Phys. Soc. Jpn. **32**, 113 (1972).
- ²² H. Hazama, T. Goto, Y. Nemoto, Y. Tomioka, A. Asamitsu, and Y. Tokura, Phys. Rev. B **62**, 15012 (2000).
- ²³ T. Watanabe, T. Ishikawa, S. Hara, A. T. M. N. Islam, E. M. Wheeler, and B. Lake, Phys. Rev. B **90**, 100407(R) (2014).
- ²⁴ Y. Nii, N. Abe, and T. Arima, Phys. Rev. B **87**, 085111 (2013).
- ²⁵ T. Watanabe, S. Yamada, R. Koborinai, and T. Katsufuji, Phys. Rev. B **96**, 014422 (2017).
- ²⁶ T. Watanabe, S. Hara, and S. Ikeda, Phys. Rev. B **78**, 094420 (2008).
- ²⁷ T. Watanabe, S. Hara, S. Ikeda, and K. Tomiyasu, Phys. Rev. B **84**, 020409(R) (2011).
- ²⁸ T. Watanabe, S. Ishikawa, H. Suzuki, Y. Kousaka, and K. Tomiyasu, Phys. Rev. B **86**, 144413 (2012).
- ²⁹ T. Watanabe, S. Takita, K. Tomiyasu, and K. Kamazawa, Phys. Rev. B **92**, 174420 (2015).
- ³⁰ Y. P. Varshni, Phys. Rev. B **2**, 3952 (1970).